Interface magnetism and anomalous Hall effect in $La_{0.7}Sr_{0.3}MnO_3/SrIrO_3$ bilayers

Andrea Peralta-Somoza,[1] Myoung Woo-Yoo,[2] Sandra Lopez,[1] Rafael Fuster,[1] Mariona Cabero,[3] José María Gonzalez-Calbet,[4] Javier Tornos,[1] Alberto Rivera ,[1] Federico Mompeán,[5,6] Mar García-Hernández,[5,6] Timothy R. Charlton,[7] Brian J. Kirby,[8] Stephan Rosenkranz,[9] Daniel Haskel,[10] Yongseong Choi,[10] Joerg Strempfer,[10] Xiao Wang,[11] Zouhair Sefrioui,[1] Carlos León,[1,6] Javier E. Villegas,[12] Suzanne G. E. te Velthuis,[9] and Jacobo Santamaría[1,6,*]

[1]*GFMC, Departamento Física de Materiales, Facultad de Física, Universidad Complutense, 28040 Madrid, Spain*
[2]*Department of Materials Science and Engineering & Materials Research Laboratory, University of Illinois Urbana-Champaign, Urbana, Illinois 61801, USA*
[3]*Centro Nacional de Microscopia Electrónica, Universidad Complutense, 28040 Madrid, Spain*
[4]*Departamento Química Inorgánica. Facultad de Química, Universidad Complutense, 28040 Madrid, Spain*
[5]*2D-Foundry Group, Instituto de Ciencia de Materiales de Madrid ICMM-CSIC, 28049 Madrid, Spain*
[6]*Laboratorio de Heteroestructuras con Aplicación en Espintrónica, ICMM-CSIC, Madrid, Spain*
[7]*Neutron Scattering Division, Oak Ridge National Laboratory, Oak Ridge, Tennessee 37831, USA*
[8]*NIST Center for Neutron Research, National Institute of Standards and Technology, Gaithersburg, Maryland 20899, USA*
[9]*Materials Science Division, Argonne National Laboratory, Lemont, Illinois 60439, USA*
[10]*Advanced Photon Source, Argonne National Laboratory, Lemont, Illinois 60439, USA*
[11]*Department of Physics, Bryn Mawr College, Bryn Mawr, Pennsylvania 19010, USA*
[12]*Laboratoire Albert Fert, Université Paris-Saclay, 91767 Palaiseau, France*

(Received 7 March 2025; accepted 7 October 2025; published 4 December 2025)

Epitaxial interfaces combining 3d and 5d transition metal oxides are a fertile playground to examine the interplay between topology and electron correlations. In this paper, we explore magnetism and transport of bilayers combining ferromagnetic $La_{0.7}Sr_{0.3}MnO_3$ and the strong spin-orbit coupling material $SrIrO_3$. We have found an interfacial magnetic proximity effect driving an intrinsic contribution to the anomalous Hall effect of topological origin. The interfacial proximity interaction is enabled by the Mn-O-Ir bonding reconstruction and depends on layer sequence. While bilayers with the $La_{0.7}Sr_{0.3}MnO_3$ on top featuring a robust Mn magnetism at the interface show the intrinsic AHE contribution, it is absent in bilayers with the inverted layer sequence ($SrIrO_3$ layer on top) showing strongly suppressed magnetism at the interface. These results illustrate the leading role of interfacial atomic reconstructions on the interplay between topology and correlations at 3d/5d oxide interfaces. This finding may be of interest in future oxide topological spintronics and spin-orbitronics.

DOI: 10.1103/qxn3-5327

I. INTRODUCTION

Interfaces between correlated oxides have been the focus of great scientific interest as they feature an attractive platform to nucleate and manipulate emergent electronic states [1,2]. In particular, the combination of 5d oxides with strong spin-orbit coupling and magnetic 3d oxides constitutes a fertile playground to examine the interplay between topology and correlations, a scenario that has gathered increasing attention in recent years [1–4]. Epitaxial oxide interfaces can be grown with atomic perfection [5], and the bonding reconstruction provides new paths for the superexchange interaction that promote exciting magnetic proximity effects [6–8]. In addition, the interplay between symmetry breaking and spin-orbit interaction may drive profound changes in the magnetic states [3]. This has opened exciting avenues for the study of a variety of interesting new phenomena, such as chiral spin textures, unconventional magnetic behaviors [1–4], and exotic proximity effects at interfaces resulting from the Dzyaloshinskii-Moriya interaction and broken inversion symmetry [3,4,9]. Apart from their fundamental interest in broadening the knowledge of quantum materials, these phenomena have a strong technological projection in next-generation spintronic and spin-orbitronic devices [10,11]. Moreover, the link between topology and electron correlations may be the seed of new responses of interest in quantum technologies, where the correlated physics brings a wide manifold of tunable responses and the topological states their robustness against external perturbations and decoherence.

In this paper, we examine the magnetism of $La_{0.7}Sr_{0.3}MnO_3/SrIrO_3$ (LSMO/SIO) interfaces. $La_{0.7}Sr_{0.3}MnO_3$ is a widely studied correlated oxide [12] with

*Contact author: jacsan@ucm.es

narrow 3d bands, which owes its half-metallic ferromagnetic state stability below room temperature to the double exchange mechanism. $SrIrO_3$ is a 5d transition metal oxide where the large octahedral crystal field stabilizes the five 5d electrons of the Ir^{4+} ions in a t_{2g}^5 low-spin configuration [13–15]. Angle-resolved photoemission spectroscopy has shown that the exotic semimetallic ground state results from heavy hole- and light electron-like bands crossing the Fermi level [16]. SIO features a unique combination of electronic correlations and strong spin-orbit coupling driven by the delicate balance between band width (kinetic energy), on-site Coulomb repulsion, and spin-orbit coupling. These three interaction terms share similar energy scales (∼0.4 eV) after the SO interaction splits the 5d band, which is otherwise rather broad. Competing kinetic energy and Coulomb repulsion in a half-filled band caused by the presence of strong SO coupling trigger a metal-insulator transition (MIT) in ultrathin films [17–19]. The coupling between the lattice and electronic sectors enabled by spin-orbit interaction endows this system with its large tunability and high sensitivity to external perturbations. We examine the interplay between the SIO's strong spin-orbit coupling and the magnetism of the LSMO as probed by measurements of the anomalous Hall effect (AHE), a transport phenomenon driven by magnetism and by the topological properties of the electronic states [20–23]. Initially ascribed to systems with finite magnetic moment, a robust AHE has also been shown to exist in antiferromagnets [24–29]. Here, we have found a surprising dependence of the AHE on the LSMO/SIO layer sequence. In LSMO (top)/SIO bilayers (with LSMO layer on top), an intrinsic component of the AHE was detected, driven by the topological properties of electronic states in momentum space (discussed in a previous publication [30]). This intrinsic contribution to the AHE was explained considering the proximity-induced magnetism within the initial 2 nm of $SrIrO_3$ at the interface. Intriguingly, in SIO (top)/LSMO (with the SIO layer on top) with the inverted layer sequence discussed in this manuscript, the interfacial intrinsic contribution to the AHE is absent. We demonstrate that this distinct behavior is governed by a strong suppression of the magnetic moment in the LSMO layer at the interface with SIO when the layer sequence is inverted. Our manuscript explains the counterintuitive result that the magnetic state of an oxide interface changes drastically by inverting the sequence of layers, which provides a direct proof that the intrinsic AHE reported in our previous publication is triggered by interfacially induced magnetism.

II. EXPERIMENTAL METHODS

A. Sample growth

The bilayers were epitaxially grown from stoichiometric $La_{0.7}Sr_{0.3}MnO_3$ (LSMO) and $SrIrO_3$ (SIO) targets by high-pressure pure oxygen sputtering at high pure oxygen pressures (2.8 mbar, or 280 Pa) and elevated temperatures (650 °C for SIO and 900 °C for LSMO). Substrates were (001)-oriented $SrTiO_3$. The high oxygen pressure growth allows for full oxidation and a high degree of thermalization of extracted species arriving to the substrate. This technique has shown epitaxial growth of oxides with good epitaxial properties [6–8].

B. STEM EELS

Aberration-corrected scanning transmission electron microscopy (STEM) and electron energy loss spectroscopy (EELS) measurements were conducted at the CNME (National Facility for Electron Microscopy at U. Complutense campus). Microscopy was conducted in a JEOL JEM ARM200cF (Certain commercial products or company names are identified here to describe our study adequately. Such identification is not intended to imply recommendation or endorsement by the National Institute of Standards and Technology) system operated at 200 kV using a condenser lens aperture of 1 mm. Cross section samples were prepared by mechanical grinding and polishing and Ar ion milling at grazing incidence in a Fischione 1010 ion mill. Samples were prepared in [100] and [110] zone axes. EELS composition analysis was performed at element-specific absorption edges (Mn $L_{2,3}$, La $M_{4,5}$, and Ir $M_{4,5}$, Sr $L_{2,3}$) using a Gatan Quantum EEL spectrometer in dual EELS mode. EELS intensities at element-specific lines were obtained from multiple linear least squares (MLLS) methods.

C. Transport measurements

The longitudinal and transverse dc resistivities, ρ_{xx} and ρ_{xy}, were measured as a function of the magnetic field H (applied perpendicular to the film plane) in the temperature range 5 K–300 K using a He fridge equipped with a superconducting magnet [Quantum Design Magnetic Properties Measurement System (MPMS)]. Hall bars (1250 × 250 mm) were patterned by optical lithography and ion etching. Voltage offsets were removed by symmetrizing (longitudinal) and antisymmetrizing (transverse) resistivity signals.

D. X-ray measurements

X-ray absorption spectroscopy (XAS) and x-ray magnetic circular dichroism (XMCD) measurements were conducted at the Advanced Photon Source (APS, Argonne National Laboratory). The Ir $L_{2,3}$ edge was probed at the APS beamline 4-ID-D (hard x-rays), where the partial fluorescence and reflectivity signals were measured. The angle of the incident beam with the sample surface was 1.5–2°, high enough to ensure that the film thickness was below the x-ray attenuation length (>250 nm) in this energy range.

E. Neutron reflectometry

Polarized neutron reflectometry was measured at the Spallation Neutron Source at Oak Ridge National Laboratory (Magnetism Reflectometer, MR) and at the NIST Center for Neutron Scattering (Polarized Beam Reflectometer, PBR). Samples were field-cooled and measured in an in-plane field of 1 T and 0.68 T for MR and PBR, respectively, and temperatures ranging between 20 K and 300 K. Reflectivity data were simultaneously fitted to models of the depth-dependent scattering length densities of the sample with temperature-independent nuclear scattering parameters, and temperature-dependent magnetic parameters using the GenX software [31,32] that is based on the Parratt formalism [33]. For some datasets, an additional nonmagnetic surface layer was necessarily included in the model to account for surface

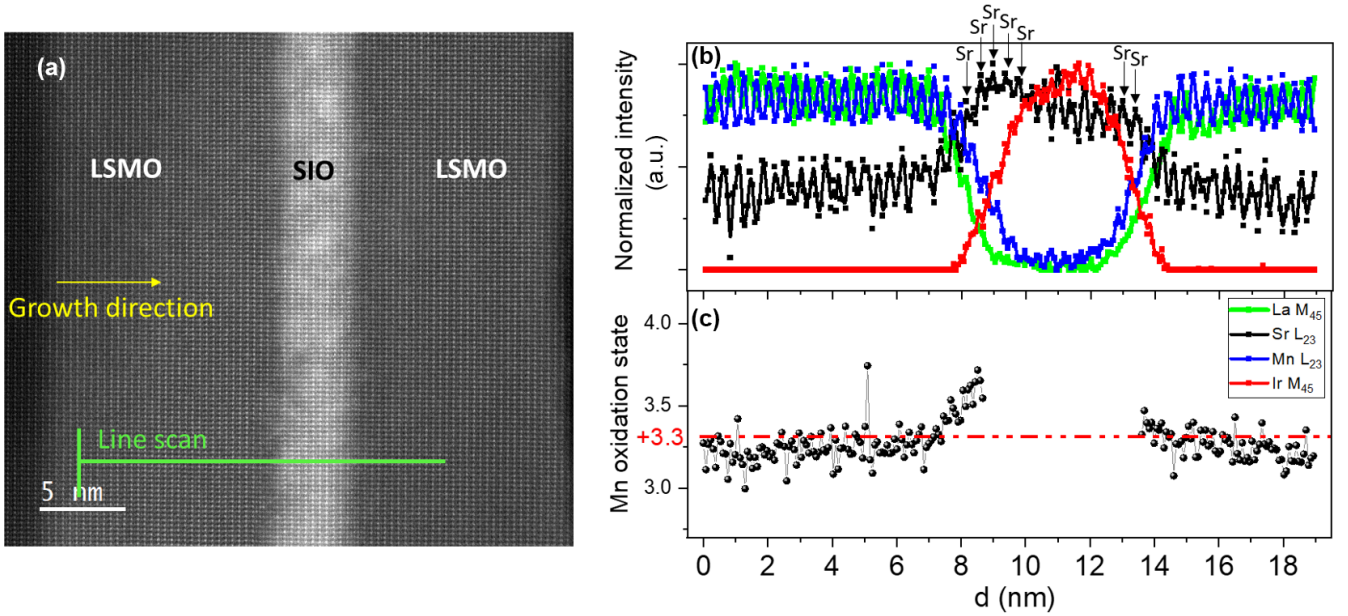

FIG. 1. Structure and chemistry of the LSMO (top)/SIO, SIO (top)/LSMO interfaces. (a) Low-magnification HAADF image of an LSMO (15 nm)/SIO (4.4 nm)/LSMO (15 nm) sample. (b) Electron energy loss (EEL) line spectrum acquired across the LSMO/SIO/LSMO interfaces following the green line over a distance d measured in nm. The yellow arrow indicates the growth direction. (c) Mn oxidation state along the green line.

contamination resulting from a slight vacuum leak of the closed cycle refrigerator holding the sample.

III. RESULTS AND DISCUSSION

In this study, we discuss two sets of samples, namely, LSMO (top) /SIO bilayers with LSMO top layers and SIO (top)/LSMO bilayers with SIO top layers. For transport measurements and AHE studies, the LSMO (top)/SIO sample set had a constant LSMO thickness of 25 nm, and the SIO thickness varied between 0 and 15 nm. The SIO (top)/LSMO samples had a constant LSMO thickness of 16 nm, and the SIO thickness varied between 0 and 15 nm. To protect the SIO layer from deterioration, samples with SIO on top were capped with a 3 nm amorphous BTO layer. It is also worth noting that probing interface magnetism required bilayer samples with thinner individual layers (see below). The slight reduction of the LSMO thickness was targeted to minimize the long-range surface roughness to ensure a good structural quality of the ultrathin SIO layer.

In a previous publication [30], we reported an intrinsic component of the anomalous Hall effect in LSMO (top)/SIO bilayers, which we ascribed to the topological properties of electronic states in momentum space. In this paper, we examine the connection between the intrinsic AHE component and interface structural electronic and magnetic reconstruction.

A. Interface structure

Aberration-corrected scanning transmission electron microscopy (STEM) was used to examine the structure and chemistry of both sets of samples. We prepared a trilayer sample LSMO (15 nm)/SIO (4.4 nm)/LSMO (15 nm), which allows examining both types of interfaces (LSMO (top)/SIO and SIO (top)/LSMO) concurrently on the same sample. Figure 1(a) features a high-angle annular dark field (HAADF) image obtained from a cross section sample thinned in the [100]/[001] plane, revealing flat and coherent interfaces. Due to contrast scaling with atomic number, the heavier Ir atoms at the B site of the perovskite (IrO_2 planes) appear brighter in the SIO, while La/Sr (A site of the perovskite) exhibit less brightness in the LSMO. Figure 1(b) presents the Mn $L_{2,3}$, La $M_{4,5}$, Sr $L_{2,3}$, and Ir $M_{4,5}$ integrated signals from an EELS line spectrum perpendicular to the interface, as indicated by the green line in Fig. 1(a). By comparing the decay of La $M_{4,5}$ and Mn $L_{2,3}$ signals toward the interfaces, it becomes evident that the bottom interface (corresponding to SIO (top)/LSMO) is MnO_2 terminated, followed by three consecutive SrO planes at the interfaces [marked with black arrows in Fig. 1(b)], yielding a MnO_2/SrO/SrO/SrO/SrO/IrO_2 layer sequence (four SrO planes with three extra SrO planes). An analysis of the Mn oxidation state from the Mn $L_{2,3}$ line (chemical) shifts evidence that, in fact, the extra SrO planes at the interface have a doping effect on the interfacial LSMO, see Fig. 1(c). It is important to remark that for a doping level in excess of $x = 3.5$, as observed, LSMO is not ferromagnetic (it is in fact antiferromagnetic) which may explain the magnetic moment suppression at the interface observed in PNR experiments and discussed below.

The top interface (corresponding to LSMO (top)/SIO) is strikingly different. It contains only two consecutive SrO planes, resulting in a MnO_2/SrO/SrO/IrO_2 layer sequence (with an additional SrO plane). For both types of interfaces, the consecutive SrO planes are laterally displaced with respect to one another, as in the rock salt structure. Additional EELS spectra at different sample locations show that while the bottom interface (LSMO on top) shows the same termination in all cases, we consistently observe a larger number of SrO

layers at the SIO top interface. Yet the number of extra SrO layers varies between three and four between different locations. An additional picture of the extra SrO layers is obtained from larger magnification cross section images of both interfaces. See Supplemental Material Fig. S1 [34]. In these images, the brighter spots correspond to the heavier elements (Ir in SIO and La in LSMO). We have marked the interfacial planes in the figure. Notice the larger interface width for the interface with SIO on top, resulting from the stacking of consecutive SrO planes, which feature a uniform contrast.

Such interface reconstructions have not been reported in other manganite iridate superlattices [35–39] grown by pulsed laser deposition (PLD) and, thus, result probably from the kinetics rather than from the thermodynamics of the growth. However, they are frequently observed at interfaces between perovskites involving different members of the Ruddlesden-Popper series [40–42].

Energetically stable structures with several rock salt layers can be found, for example, in cuprates where double, triple, or quadruple rock salt layers are frequently found [43,44] or engineered on purpose at titanate interfaces by layer-by-layer thin film growth [45]. The formation of additional SrO planes can be discussed in connection with Ruddlesden–Popper non-stoichiometric defects as (SrO)2 faults have a lower formation energy than that of a point defect [46] or with strain relaxation, which is denounced by varying distances between consecutive SrO planes in blocks with an arbitrary number of SrO planes [45]. Charge imbalance can be ruled out as SrO blocks are charge neutral and do not contribute to layer polarity.

Similar to other manganite-based heterostructures [42], the interfacial SrO planes will profoundly impact the electronic structure. Moreover, the presence of a different number of interfacial SrO planes in bilayers with both stacking sequences impacts the bonding structure, thus deeply modifying the electronic and magnetic structure.

B. Polarized neutron reflectometry

Polarized neutron reflectometry (PNR) was measured with the incident neutron polarization parallel (R^+) and antiparallel (R^-) to the magnetic field for a LSMO (5 nm)(top)/SIO (4 nm) [see Figs. 2(a) and 2(b)] and an SIO (4 nm)(top)/LSMO (5 nm) bilayer with an amorphous $BaTiO_3$ capping layer [Figs. 2(c) and 2(d)]. The small thickness of the individual layers ensures large interface sensitivity and allows comparison with the x-ray absorption spectroscopy measurements of the next section. Samples were field-cooled and measured in a saturating in-plane magnetic field in the 1 T range and at 7 or 8 temperatures ranging between 20 K and 300 K, see Sec. II.

Reflectivity spectra at T = 20 K are displayed in Fig. 2(a) for LSMO(top)/SIO and Fig. 2(c) SIO (top)/LSMO samples. The PNR spectra were fit using an iterative Parratt algorithm [31–33] to obtain the nuclear and magnetic scattering length densities (SLD) as a function of the height above the STO substrate. The magnetic SLD is proportional to the layer magnetization. Reflectivity data measured at different temperatures were simultaneously fit to a model with temperature-dependent magnetic SLDs, but a single nuclear SLD profile describing the sample, allowing for a robust determination of the SLD profiles. The SLD profiles, corresponding to the fits of the spectra in Figs. 2(a) and 2(c), are shown in Figs. 2(b) and 2(d), respectively. Notice that when SIO is the top layer [Fig. 2(d)], the magnetization of LSMO is drastically suppressed from 0.53×10^6 to 0.03×10^6 A/m at the interface over a thickness of 1.3 nm. In contrast, when LSMO is the top layer, there is only a weak reduction of the magnetization from 0.62×10^6 to 0.51×10^6 A/m at the interface over 0.6 nm.

Although the Q-range of the data for the SIO (top)/LSMO sample [Fig. 2(c)] is limited, the fit of data collected at T = 100 K, that extends up to Q = 1.8 nm^{-1} shows the same strong suppression of the magnetization at the interface (see Supplemental Material Fig. S2, panels (a), (c), and (e) [34]). If the magnetization of LSMO is constrained to be homogeneous throughout the entire layer, the fits deviate significantly from the data, even within the limited Q-range of the 20 K dataset (see Supplemental Material Fig. S2 panels (b), (d), and (f) [34]). The suppression of LSMO magnetization observed at the SIO (top)/LSMO interface can be related to the doping effect of the extra SrO planes discussed above, which brings the oxidation state of Mn at the interface well above 3.5, the limit above which the manganite becomes an antiferromagnet [47,48].

C. X-ray absorption spectroscopy

Although SIO is a paramagnetic compound, the bonding reconstruction at the interface can be the source of proximity-induced Ir magnetism through superexchange interaction along a Mn-O-Ir path. Interfacial Ir magnetism was investigated using x-ray absorption spectroscopy (XAS) and x-ray magnetic circular dichroism (XMCD) at the Ir $L_{2,3}$ edges in the same LSMO (top)/SIO and SIO (top)/LSMO bilayers used for the PNR experiments. Figure 3 illustrates the Ir L_3 edge XAS (top) and XMCD (bottom) for the LSMO (5 nm)/SIO (4 nm) bilayer and the SIO (4 nm)/LSMO (5 nm) bilayer with an amorphous $BaTiO_3$ capping layer at 20 K and 55.5 mT. XMCD spectra in partial fluorescence yield (PFY) mode displayed clear evidence of an Ir magnetic moment for the LSMO (top)/SIO bilayer. In contrast, the SIO (top)/LSMO bilayer with SIO on top does not exhibit an Ir magnetic moment. The origin of the Ir magnetic state found in LSMO(top)/SIO bilayers, which as reported earlier extends over 2 nm from the interface [30], can be discussed in relation to the magnetic moment of the interfacial LSMO. On the other hand, the absence of Ir magnetic moment in the SIO (top)/LSMO bilayers may be attributed to the suppressed LSMO magnetism at the interface resulting from the atomic reconstruction of the interface uncovered by the STEM-EELS experiment.

Induced magnetism in iridates has been reported in manganite/iridate superlattices with various interface reconstructions [34–38,49], although significant differences arise from our unique LSMO/SIO interface reconstruction, as discussed below. The small values of the spin and orbital magnetic moments found in application of the sum rules [30,50] using L_2 and L_3 edge data at 20 K (spin moment $\langle S_z \rangle = 0.003\,\mu_B$ and orbital moment $\langle L_z \rangle = 0.018\,\mu_B$), which

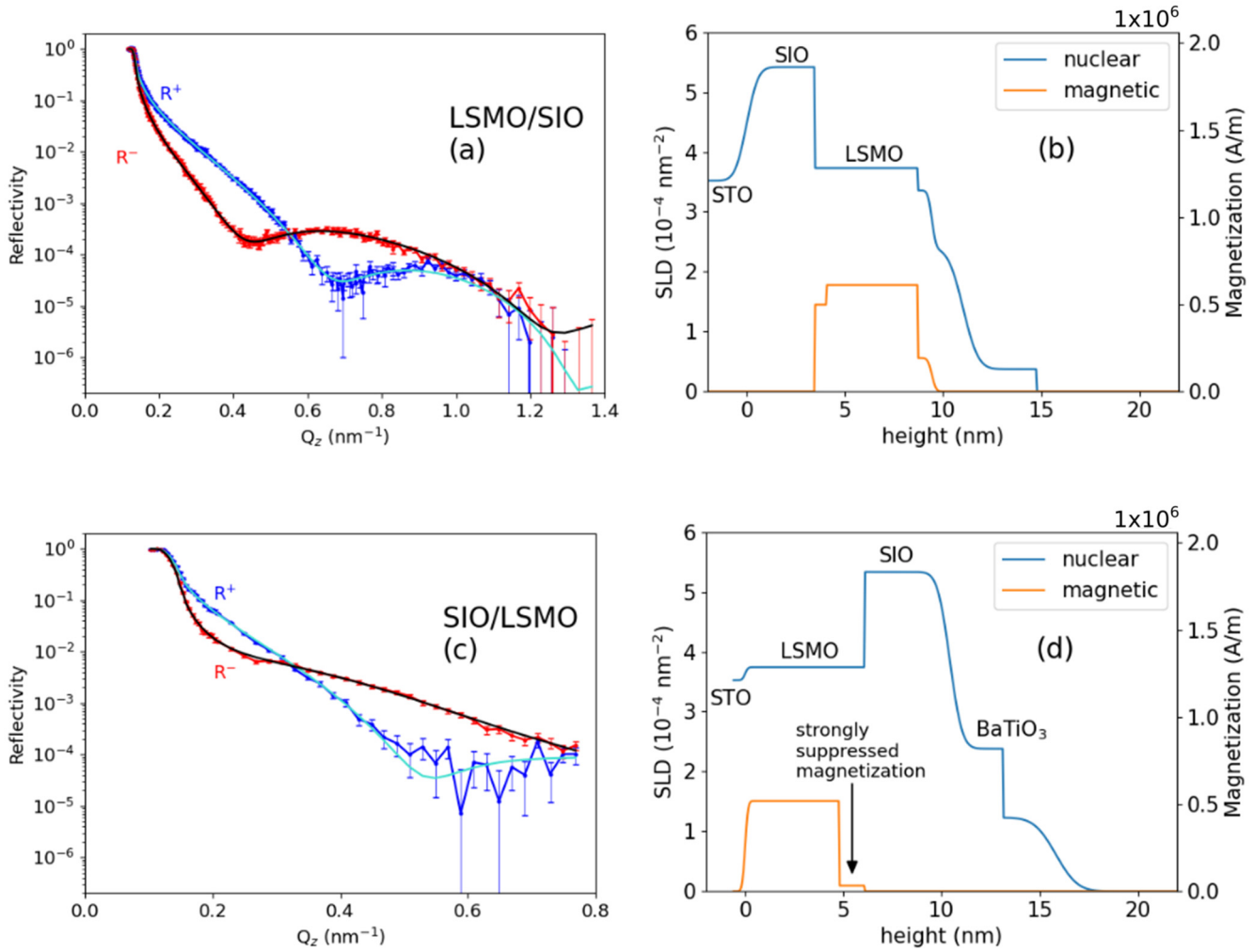

FIG. 2. (a), (c) Polarized neutron reflectivity data (markers) and fits (lines) as a function of momentum transfer Q_z, measured at 20 K in saturating in-plane magnetic fields, 1 T, after field cooling for a LSMO(5 nm)(top)/SIO (4nm) [panel (a)] and for a SIO (4 nm)(top)/LSMO(5 nm)(bottom) bilayer with a $BaTiO_3$ capping layer [panel (c)]. The fits are calculations of the reflectivity based on the scattering length density (SLD) profiles shown in panels (b) and (d). (b), (d) Nuclear and magnetic scattering length density as a function of the height above the STO substrate surface for a LSMO (5 nm)(top)/SIO (4nm) (panel b) and for a SIO (4 nm)(top)/LSMO(5 nm)(bottom) bilayer with a $BiTiO_3$ cap [panel (d)]. The right *y*-axis provides the magnetization calculated from the magnetic scattering length density.

were aligned antiparallel to the Mn moment, are typical of a canted antiferromagnetic state. We attribute the origin of the small induced magnetic moment in the SIO layer (observed in the LSMO (top)/SIO interface) to canting of the interfacial SIO-214 unit cell resulting from the presence of a single extra SrO plane at the interface. In this scenario, the canted antiferromagnetic (AFM) ordering would be driven by the Dzyaloshinskii-Moriya interaction [51–54], which is dominant when the local Coulomb repulsion U on Ir d states exceeds ∼1 eV [30]. I.e., the LSMO in proximity to SIO-214 induces the canted antiferromagnetic state in a way driven by enhanced electron correlations. Given the small energy difference between various canted AFM states (less than ∼10 meV/Ir), the weak superexchange interaction [6,8,55,56] across the double SrO layers, as evidenced by the antiferromagnetic alignment of the Mn and Ir moments [30], is sufficient to produce the observed magnetic state. It is noteworthy that this superexchange interaction across double SrO layers has been observed in $La_{1.85}Sr_{0.15}CuO_4$ (LSCO-214) cuprate/manganite interfaces [42], where it also results in an antiferromagnetic (Cu-Mn) state. It is also worth mentioning that this weak ferromagnetism has been shown to survive in SIO/STO superlattices with one unit cell thick SIO layers [50–53]. The suppressed Mn magnetism at the SIO (top)/LSMO interface naturally explains the absence of an induced Ir moment.

D. Transport

The temperature dependence of the longitudinal resistivity measured on 16 and 25 nm LSMO control samples displayed the same values for both thicknesses. The effect of adding the SIO layers was an overall increase in the longitudinal resistivity due to the contribution of the more resistive SIO layers.

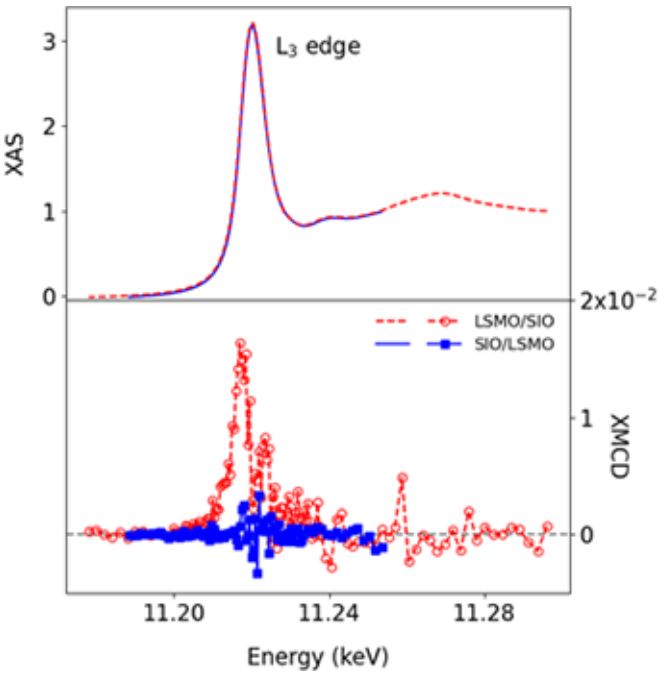

FIG. 3. Ir L_3 XAS (lines, top panel) and XMCD (markers, bottom panel) partial fluorescence yield PFY spectra measured at T = 20 K under a saturating magnetic field of 55.6 mT applied in the [100] direction of a samples LSMO(5nm)/SIO(4nm) (red circles) and SIO (4 nm)/LSMO (5 nm) with a $BiTiO_3$ capping layer (blue squares).

We measured the temperature dependence of the transverse resistivity ρ_{xy}. Figure 4 shows the transverse resistivity measurements between 20 and 100 K for LSMO/SIO and SIO/LSMO bilayers for different thicknesses of the SIO layer. The contributions of the ordinary Hall effect (OHE) and of the anomalous Hall effect (AHE) ($\rho_{xy} = \rho_{xy}^{\mathrm{OHE}} + \rho_{xy}^{\mathrm{AHE}}$) can be readily identified. Notice that the OHE is proportional to the magnetic field (H_z), while the AHE is proportional to the magnetization (M_z) perpendicular to the film plane.

Hall effect measurements on control LSMO (16 and 25 nm thick) and SIO individual layers at temperatures T $\leqslant$ 100 K are presented in Fig. 5. The sign of the OHE in LSMO (hole carriers) is opposite to that in SIO (electron carriers).

The AHE contribution can be isolated by correcting measurements for the linear OHE contribution. For pristine LSMO films with a ferromagnetic ground state, ρ_{xy}^{AHE} becomes constant once M_z is saturated by the applied field H_z (red line in Fig. 5).

On the other hand, in the SIO films, which have a paramagnetic ground state, a null ρ_{xy}^{AHE} is found. From the excess value ($\Delta\rho_{xy}^{\mathrm{AHE}}$) of ρ_{xy}^{AHE} at magnetic saturation (marked by the green arrows in Fig. 5) we can quantify the anomalous Hall conductivity. Notice that although LSMO samples of different thicknesses behave qualitatively similarly, larger values of $\Delta\rho_{xy}^{\mathrm{AHE}}$ (by a factor of 3) are obtained for the thicker 25 nm sample, a difference which cannot be attributed to different resistivity. In manganite single crystals [57] or thick epitaxial films [58], AHE is negligibly small below 100 K and increases rapidly with temperature when the MIT is approached. In thin films, the low-temperature AHE is typically nonzero and its value changes substantially from sample to sample in a way (to our knowledge) that is not well understood.

We next examine the AHE $\Delta\rho_{xy}^{\mathrm{AHE}}$ for both sets of samples (LSMO (top)/SIO and SIO (top) /LSMO) for T $\leqslant$ 100 K, a temperature range where saturation magnetization remains essentially constant. We have measured SQUID magnetometry of an LSMO sample 20 nm thick (representative of the LSMO layers of both series of samples with special attention to the temperature dependence of the saturation magnetization. Supplemental Material Fig. S3 [34] gathers M(T) for in-plane and out-of-plane fields [panel (a)] and M(B) loops under in-plane [panel (b)] and out-of-plane [panel (c)] magnetic fields. It can be observed that below 100 K magnetization shows a weak temperature dependence. Thus, since AHE is proportional to magnetization and to AH conductivity, changes in AHE for temperatures T < 100 K can be attributed to changes in the anomalous Hall conductivity. At higher temperatures, despite the decrease of magnetization, it displays a strong increase when the metal-to-insulator transition is approached; the origin is not addressed in this work.

Plots of $\Delta\rho_{xy}^{\mathrm{AHE}}(T)$ against $\rho_{xx}^2(T)$ for the two bilayer sets, SIO/LSMO [Fig. 6(a)] and LSMO/SIO [Fig. 6(b)] for different values of the SIO thickness (d_S), are displayed in Fig. 6. For both sets, a linear scaling is observed over the entire range of d_S, including the sample without SIO ($d_S = 0$):

$$\Delta\rho_{xy}^{\mathrm{AHE}}(T) = \left|\sigma_{xy}^{\mathrm{AHE}}\right| \cdot \rho_{xx}^2(T). \tag{1}$$

This finding suggests that the anomalous Hall conductivity, $\sigma_{xy}^{\mathrm{AHE}}$, is independent of the scattering rate, and thus, the observed AHE is of intrinsic origin, i.e., driven by the topological properties of electron states in reciprocal space [21] as discussed previously [30]. In fact, $\sigma_{xy}^{\mathrm{AHE}}$ can be expressed as the integral of the Berry phase curvature over occupied states in the Brillouin zone [20,22,23].

Notice that the lines corresponding to the pristine LSMO samples have smaller slopes for the SIO /LSMO (16 nm) bilayers than for the LSMO (25 nm)/SIO ones, reflecting the smaller values of the anomalous Hall resistivity $\Delta\rho_{xy}^{\mathrm{AHE}}$ and correspondingly lower values of the anomalous Hall conductivity. In addition, the relative change of the slopes when the SIO thickness is increased is considerably larger in the LSMO (25 nm)/SIO samples, suggesting a different contribution to the anomalous Hall conductivity for both sets of samples. Figure 7 displays the dependence of the anomalous Hall conductivity $\sigma_{xy}^{\mathrm{AHE}}$ on SIO thickness (obtained from the slopes of the $\Delta\rho_{xy}^{\mathrm{AHE}}$ vs ρ_{xx}^2 of Fig. 6) for both the SIO (top)/LSMO and LSMO (top)/SIO bilayers. Since the difference in the AHE resistivity for both sets of samples yields differences in the anomalous Hall conductivity for the pristine (25 and 16 nm) LSMO samples, to compare the effect of increasing the SIO thickness on the anomalous Hall conductivity (Fig. 7), both sets have been normalized to the (respective) plain manganite values. The value of the AH resistivity of pristine LSMO layers is very small in the T < 100 K range and might be prone to sample variation and data processing. Notice that while the $\sigma_{xy}^{\mathrm{AHE}}$ for the LSMO/SIO bilayers displays an abrupt decrease when d_S is increased, followed by a quick saturation, the SIO/LSMO bilayers exhibit a more gradual, weaker, and

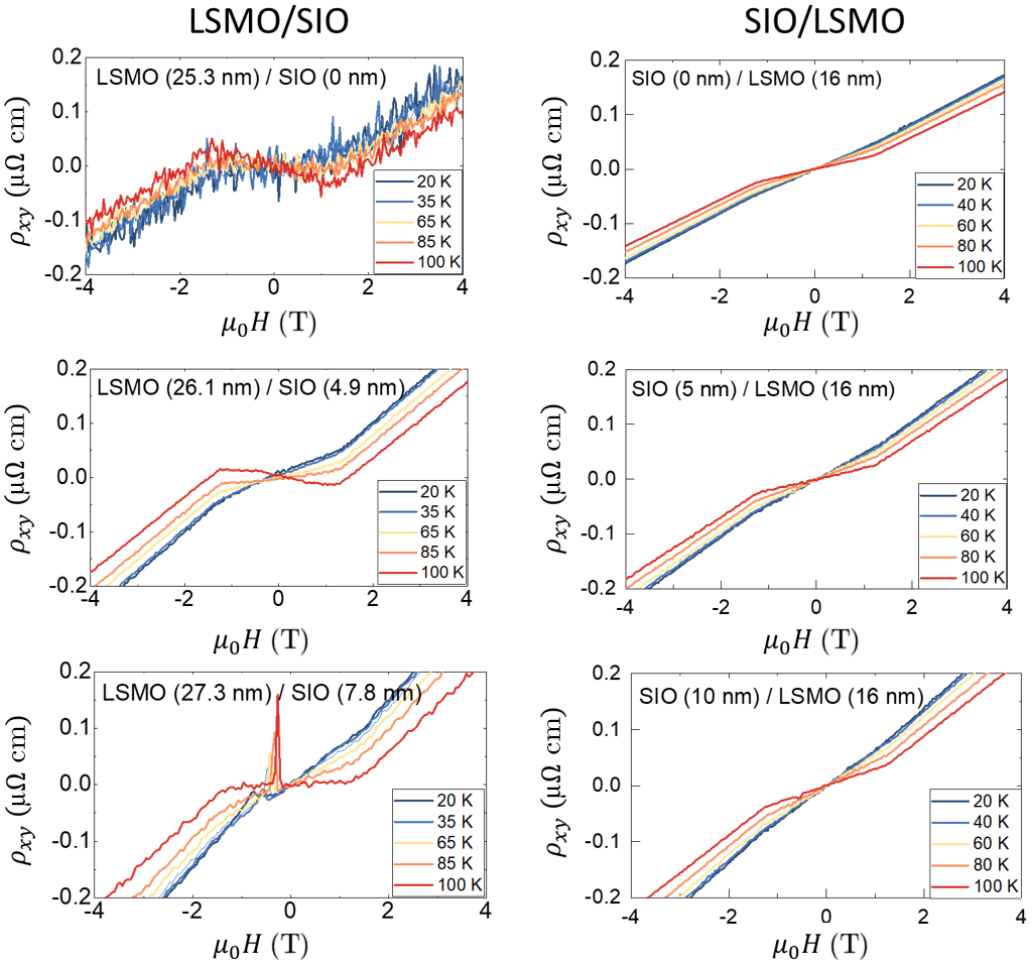

FIG. 4. Transverse Hall resistivity ρ_{xy} vs out-of-plane magnetic field, H_z, at temperatures between 20 K and 100 K in bilayers LSMO/SIO (left panels) and bilayers SIO/LSMO (right panels) for different thicknesses of the SIO layer.

steadier decrease of $\sigma_{xy}^{\mathrm{AHE}}$ as the thickness (d_S) of the SIO layer is increased.

The dependence of the anomalous Hall conductivity of the bilayers on the SIO layer thickness was analyzed, using a parallel layer model which describes the transverse ρ_{xy}^{AHE} and longitudinal ρ_{xx} resistivity of a multilayer in terms of their values for the individual layers [59,60]. As the AHE conductivity scales as $\sigma_{xy}^{\mathrm{AHE}} = \Delta\rho_{xy}^{\mathrm{AHE}}/\rho_{xx}^2$, to model its behavior in the heterostructure, we need to describe the total longitudinal resistivity, ρ_{xx}, and anomalous Hall resistivity, $\Delta\rho_{xy}^{\mathrm{AHE}}$, as a function of the contributions of the different layers. AHE conductivity $\sigma_{xy}^{\mathrm{AHE}}$

$$\sigma_{xy}^{\mathrm{AHE}} = \frac{\Delta\rho_{xy}^{\mathrm{AHE}}}{\rho_{xx}^2} = \frac{\sum_{i=1}^{n} d_i\, \sigma_{xy,i}^{\mathrm{AHE}}}{\sum_{i=1}^{n} d_i}. \qquad (2)$$

Here, $\Delta\rho_{xy}^{\mathrm{AHE}}$ and ρ_{xx} represent the anomalous Hall and longitudinal resistivity expected in measurements on a

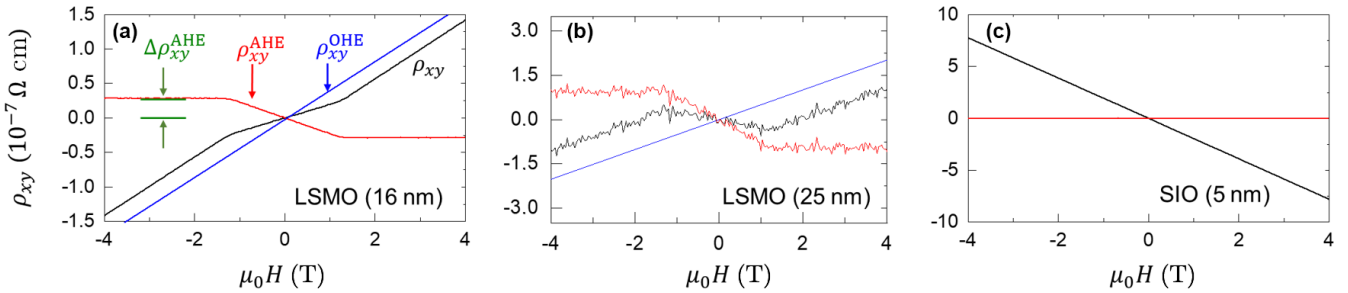

FIG. 5. Transverse Hall resistivity ρ_{xy} vs out-of-plane magnetic field, H, (black lines) of LSMO 16 nm (a), LSMO 25 nm (b), and SIO 5 nm (c) control samples measured at T = 100 K. Ordinary Hall resistivity, ρ_{xy}^{OHE}, (blue lines) and anomalous Hall resistivity, ρ_{xy}^{AHE}, (red lines) contributions to the transverse resistivity have been separated. $\Delta\rho_{xy}^{\mathrm{AHE}}$ (in green) indicates the value of ρ_{xy}^{AHE} at magnetic saturation.

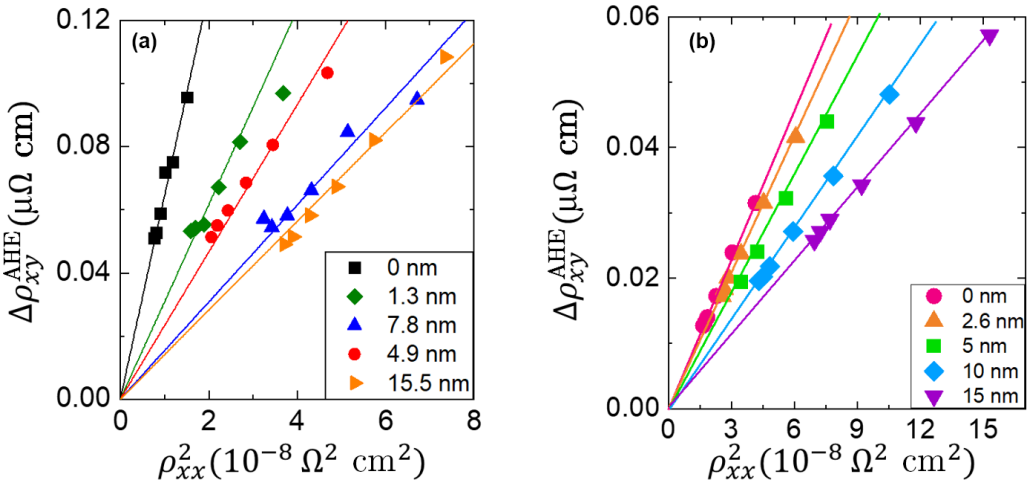

FIG. 6. Dependence of the AHE at saturation, $\Delta\rho_{xy}^{AHE}$ on the longitudinal resistivity, ρ_{xx}^2, at temperatures below 100 K for LSMO (25 nm)/SIO bilayers (right) and SIO/LSMO (16 nm) bilayers (left) for different thicknesses of SIO (see legend). Data of the LSMO (25 nm)/SIO bilayer are taken from Ref. [30].

heterostructure composed of n different layers, with each layer having a thickness d_i and anomalous Hall conductivity $\sigma_{xy,i}^{AHE} = \Delta\rho_{xy,i}^{AHE}/\rho_{xx,i}^2$. This analysis is described in detail in Ref. [30].

If we assume that both materials retain their intrinsic AHE resistivity when combined in the heterostructures—i.e., only LSMO displays a finite $\sigma_{xy,L}^{AHE}$ while the SIO layer has $\sigma_{xy,S}^{AHE} = 0$ are as depicted in Fig. 5—and considering that LSMO and SIO layers have thicknesses that d_L, d_S respectively, then Eq. (2) yields

$$\sigma_{xy}^{AHE} = \frac{d_L}{d_L + d_S}\sigma_{xy,L}^{AHE}. \tag{3}$$

For the SIO (top)/LSMO bilayers, we find that Eq. (3) accounts well for experimental results (purple dotted line in Fig. 7), indicating that these samples preserve their intrinsic AHE conductivity when assembled in a heterostructure. I.e., the AHE probe does not detect any modification of the topological properties of electronic states in momentum space. In contrast, for the LSMO (top)/SIO bilayers, fitting the data requires including a magnetic SIO layer at the interface, as we described in our previous paper [30]. Assuming that the magnetic SIO layer has a thickness d_I, we can write the following expression for the anomalous Hall conductivity:

$$\sigma_{xy}^{AHE} = \frac{d_L\sigma_{xy,L}^{AHE} + d_I\sigma_{xy,I}^{AHE}}{d_L + d_S}. \tag{4}$$

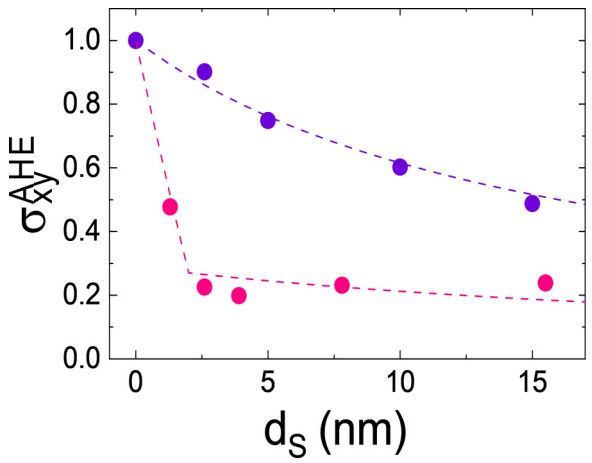

FIG. 7. Normalized values of the AHE conductivity, σ_{xy}^{AHE}, vs thickness of the SIO layer, for SIO/LSMO (purple symbols) and LSMO/SIO (pink symbols) bilayer samples. Values of the Hall conductivity have been obtained from the linear fits of Fig. 3. The purple dashed line indicates the calculated σ_{xy}^{AHE} using the parallel layer model described below, Eq. (3). The pink dashed line indicates the calculated σ_{xy}^{AHE}AHExy using a trilayer model, Eq. (4).

Given that d_L, d_S, σ_{xy}^{AHE}, and $\sigma_{xy,L}^{AHE}$ are known parameters, and that $d_I \sim 2$ nm was independently obtained from the dependence of the interfacial Ir magnetic moment (determined from XMCD spectra at the Ir L-edge) on the thickness of the SIO layer [30], we can estimate the anomalous Hall conductivity of magnetic SIO layer, $\sigma_{xy,I}^{AHE}$, by fitting the data using Eq. (4) (see pink dotted line in Fig. 7). Thus, our analysis using the three-layer model identifies an intrinsic contribution to the AHE conductivity, $\sigma_{xy,I}^{AHE} \sim -60\,(\Omega\,\mathrm{cm})^{-1}$, which is negative and nearly independent of d_S as reported earlier [30]. The large absolute value of $\sigma_{xy,I}^{AHE}$ along with its scattering rate independence, strongly suggests its intrinsic origin—namely, the topological nature of the Bloch states in SIO in momentum space, specifically the Berry curvature of the occupied states [21]. It is worth pointing out that such a high value of $\sigma_{xy,I}^{AHE}$ is comparable to that found for $SrRuO_3$ [61] MnSi [62,63], and the noncollinear antiferromagnets Mn_3Sn [26] or $CoNb_3S_6$ [64] with topologically nontrivial bands. However, it is much larger than the values found in LSMO with topologically trivial bands, where carriers acquire a real-space Berry phase due to noncollinear spin structures, predominantly near T_C [57,65].

A final comment is in order regarding the smaller thickness of the individual layers necessary to probe interface magnetism with x-ray absorption and PNR. Although the transport experiments are done in bilayers with

thicker layers well above the thickness where dead layers may trigger modifications in the LSMO layer magnetism, we checked that bilayers with these smaller thicknesses show the same modulation of the intrinsic anomalous Hall effect by proximity-induced magnetism at the interface. Supplemental Material Fig. S4 [34] shows that even for very thin LSMO (3.5 nm) and SIO (2.4 nm), the strong suppression of the anomalous Hall conductivity in LSMO (top)/SIO bilayers ($\sigma_{AHE} = 0.081\,\Omega^{-1}\,cm^{-1}$) with respect to plain 3.5 nm thick LSMO ($\sigma_{AHE} = 0.456\,\Omega^{-1}\,cm^{-1}$) is more pronounced than in SIO (top)/LSMO ($\sigma_{AHE} = 0.28\,\Omega^{-1}\,cm^{-1}$), where current splitting between layers is expected to be the dominant mechanism. Moreover, notice that this value ($\sigma_{AHE} = 0.28\,\Omega^{-1}\,cm^{-1}$) is very close to the expected from the layer thickness ratio according to Eq. (3).

This intrinsic contribution to the anomalous Hall conductivity found at the LSMO (top)/SIO interface is not observed in the SIO (top)/LSMO bilayers, and it is thus connected to the presence of magnetism in the interfacial LSMO, and consequently of the induced magnetism in the first 2 nm of SIO [30]. Only the induced magnetism in Ir, characteristic of the LSMO (top)/SIO interface, allows for the interplay between topology and correlations in which the large intrinsic AHE emerges despite the small values of the magnetic moment induced by the interfacial proximity interaction.

IV. CONCLUSIONS

In summary, we have found an intriguing magnetic proximity effect at $La_{0.7}Sr_{0.3}MnO_3/SrIrO_3$ resulting from the chemical and bonding reconstruction at the interface, driven by the nucleation of a rocksalt $(SrO)_n$ block at the interface and by the superexchange interaction across it. An emergent AHE is found in $La_{0.7}Sr_{0.3}MnO_3/SrIrO_3$ bilayers with LSMO on top, where LSMO magnetism is preserved down to the interface plane, allowing for induced magnetism in the iridate. This AHE contribution is absent in bilayers with the opposite layer sequence (SIO layer on top), where LSMO magnetism is suppressed at the interface and, consequently, the magnetic proximity interaction is absent. The intrinsic AHE of topological origin uncovers an exciting scenario of interplay between topology and correlations at the 3d/5d interface, enabled by magnetic proximity interaction, and may open new avenues to future topological spintronics and spin orbitronics.

ACKNOWLEDGMENTS

Work at UCM and Laboratoire Albert Fert was supported by the 2020 research and innovation program under the EIC Pathfinder Grant No. 101130224 "JOSEPHINE," and COST action "SUPERQUMAP." Work at UCM was supported by Agencia Estatal de Investigación through Grants No. PID2023-148884OB-I00 and No. 2021–130196B-C21, and by the "(MAD2D-CM)-UCM" project funded by Comunidad de Madrid, by the Recovery, Transformation and Resilience Plan, and by NextGenerationEU from the European Union. Work at CNRS/Thales supported by French ANR "SUPERFAST" and "SUPERSPIN" through the France 2030 government grant PEPR-SPIN ANR-24-EXSP-0012. Work at Bryn Mawr was supported by NSF (Grant No. DMR #1708790). Work by S.G.E.t.V. and S.R. (neutron and x-ray experiments and analysis) was supported by the U.S. Department of Energy, Office of Science, Basic Energy Sciences, Materials Sciences and Engineering Division. This research used resources of the Advanced Photon Source, a U.S. Department of Energy (DOE) Office of Science User Facility operated for the DOE Office of Science by Argonne National Laboratory under Contract No. DE-AC02-06CH11357. This research used resources at the Spallation Neutron Source, a DOE Office of Science User Facility operated by the Oak Ridge National Laboratory.

DATA AVAILABILITY

The data that support the findings of this article are not publicly available upon publication because it is not technically feasible, and/or the cost of preparing, depositing, and hosting the data would be prohibitive within the terms of this research project. The data are available from the authors upon reasonable request.

[1] Y. Tokura, M. Kawasaki, and N. Nagaosa, Emergent functions of quantum materials, Nat. Phys. **13**, 1056 (2017).
[2] B. Keimer and J. E. Moore, The physics of quantum materials, Nat. Phys. **13**, 1045 (2017).
[3] W. Witczak-Krempa, G. Chen, Y. B. Kim, and L. Balents, Correlated quantum phenomena in the strong spin-orbit regime, Annu. Rev. Condens. Matter Phys. **5**, 57 (2013).
[4] A. Soumyanarayanan, N. Reyren, A. Fert, and C. Panagopoulos, Emergent phenomena induced by spin-orbit coupling at surfaces and interfaces, Nature (London) **539**, 509 (2016).
[5] H. Boschker and J. Mannhart, Quantum-matter heterostructures, Annu. Rev. Condens. Matter Phys. **8**, 145 (2017).
[6] J. Garcia-Barriocanal *et al.*, Spin and orbital Ti magnetism at $LaMnO_3/SrTiO_3$ interfaces, Nat. Commun. **1**, 82 (2010).
[7] F. A. Cuellar *et al.*, Reversible electric-field control of magnetization at oxide interfaces, Nat. Commun. **5**, 4215 (2014).
[8] F. Y. Bruno *et al.*, Insight into spin transport in oxide heterostructures from interface-resolved magnetic mapping, Nat. Commun. **6**, 6306 (2015).
[9] A. Gariglio, S. D. Caviglia, A. D. Triscone, and J. M. Gabay, A spin-orbit playground: Surfaces and interfaces of transition metal oxides, Rep. Prog. Phys. **82**, 12501 (2019).
[10] M. Bibes, J. E. Villegas, and A. Barthélèmy, Ultrathin oxide films and interfaces for electronics and spintronics, Adv. Phys. **60**, 5 (2011).
[11] R. Ramesh and D. G. Schlom, Creating emergent phenomena in oxide superlattices, Nat. Rev. Mater. **4**, 257 (2019).
[12] M. Imada, A. Fujimori, and Y. Tokura, Metal-insulator transitions, Rev. Mod. Phys. **70**, 1039 (1998).
[13] S. J. Moon *et al.*, Dimensionality-controlled insulator-metal transition and correlated metallic state in 5*d* transition metal oxides $Sr_{n+1}Ir_nO_{3n+1}$ ($n = 1$, 2, and ∞), Phys. Rev. Lett. **101**, 226402 (2008).

[14] B. J. Kim, H. Ohsumi, T. Komesu, S. Sakai, T. Morita, H. Takagi, and T. Arima, Phase-sensitive observation of a spin-orbital Mott state in Sr_2IrO_4, Science **323**, 1329 (2009).

[15] J. Liu *et al.*, Tuning the electronic properties of $J_{\text{eff}} = 1/2$ Correlated semimetal in epitaxial perovskite $SrIrO_3$, arXiv:1305.1732.

[16] Y. F. Nie *et al.*, Interplay of spin-orbit interactions, dimensionality, and octahedral rotations in semimetallic $SrIrO_3$, Phys. Rev. Lett. **114**, 016401 (2015).

[17] D. J. Groenendijk *et al.*, Spin-orbit semimetal $SrIrO_3$ in the two-dimensional limit, Phys. Rev. Lett. **119**, 256403 (2017).

[18] P. Schütz *et al.*, Dimensionality-driven metal-insulator transition in spin-orbit-coupled $SrIrO_3$, Phys. Rev. Lett. **119**, 256404 (2017).

[19] F. Gallego *et al.*, Reversible metal-insulator transition in $SrIrO_3$ ultrathin layers by field effect control of inversion symmetry breaking, Commun. Mater. **4**, 36 (2023).

[20] N. Nagaosa, J. Sinova, S. Onoda, A. H. MacDonald, and N. P. Ong, Anomalous Hall effect, Rev. Mod. Phys. **82**, 1539 (2010).

[21] F. D. M. Haldane, Berry curvature on the Fermi surface: Anomalous Hall effect as a topological Fermi-liquid property, Phys. Rev. Lett. **93**, 206602 (2004).

[22] S. Onoda, N. Sugimoto, and N. Nagaosa, Intrinsic versus extrinsic anomalous Hall effect in ferromagnets, Phys. Rev. Lett. **97**, 126602 (2006).

[23] S. Onoda, N. Sugimoto, and N. Nagaosa, Quantum transport theory of anomalous electric, thermoelectric, and thermal Hall effects in ferromagnets, Phys. Rev. B **77**, 165103 (2008).

[24] H. Chen, Q. Niu, and A. H. Macdonald, Anomalous Hall effect arising from noncollinear antiferromagnetism, Phys. Rev. Lett. **112**, 017205 (2014).

[25] J. Kübler and C. Felser, Non-collinear antiferromagnets and the anomalous Hall effect, Europhys. Lett. **108**, 67001 (2014).

[26] S. Nakatsuji, N. Kiyohara, and T. Higo, Large anomalous Hall effect in a non-collinear antiferromagnet at room temperature, Nature (London) **527**, 212 (2015).

[27] N. Kiyohara, T. Tomita, and S. Nakatsuji, Giant anomalous Hall effect in the chiral antiferromagnet Mn_3Ge, Phys. Rev. Appl. **5**, 064009 (2015).

[28] A. K. Nayak *et al.*, Large anomalous Hall effect driven by a nonvanishing Berry curvature in the noncolinear antiferromagnet Mn_3Ge, Sci. Adv. **2**, e1501870 (2016).

[29] L. Šmejkal, A. H. MacDonald, J. Sinova, S. Nakatsuji, and T. Jungwirth, Anomalous Hall antiferromagnets, Nat. Rev. Mater. **7**, 482 (2021).

[30] M. W. Yoo *et al.*, Large intrinsic anomalous Hall effect in $SrIrO_3$ induced by magnetic proximity effect, Nat. Commun. **12**, 3283 (2021).

[31] M. Björck and G. Andersson, *GenX:* An extensible X-ray reflectivity refinement program utilizing differential evolution, J. Appl. Crystallogr. **40**, 1174 (2007).

[32] A. Glavic and M. Björck, *GenX 3:* The latest generation of an established tool, J. Appl. Crystallogr. **55**, 1063 (2022).

[33] L. G. Parratt, Surface studies of solids by total reflection of x-rays, Phys. Rev. **95**, 359 (1954).

[34] See Supplemental Material at http://link.aps.org/supplemental/10.1103/qxn3-5327 for supplemental figures.

[35] D. Yia *et al.*, Atomic-scale control of magnetic anisotropy via novel spin-orbit coupling effect in $La_{2/3}Sr_{1/3}MnO_3/SrIrO_3$ superlattices, Proc. Natl. Acad. Sci. USA **113**, 6397 (2016).

[36] J. Nichols *et al.*, Emerging magnetism and anomalous Hall effect in iridate-manganite heterostructures, Nat. Commun. **7**, 12721 (2016).

[37] D. Yi *et al.*, Tuning perpendicular magnetic anisotropy by oxygen octahedral rotations in $(La_{1-x}Sr_xMnO_3)/(SrIrO_3)$ superlattices, Phys. Rev. Lett. **119**, 077201 (2017).

[38] Y. Li, L. Zhang, Q. Zhang, C. Li, T. Yang, Y. Deng, L. Gu, and D. Wu, Emergent topological Hall effect in $La_{0.7}Sr_{0.3}MnO_3/SrIrO_3$ heterostructures, ACS Appl. Mater. Interfaces **11**, 21268 (2019).

[39] E. Skoropata *et al.*, Interfacial tuning of chiral magnetic interactions for large topological Hall effects in $LaMnO_3/SrIrO_3$ heterostructures, Sci. Adv. **6**, eaaz3902 (2020).

[40] M. Matvejeff, T. Chikyow, and M. Lippmaa, Interface growth of $La_{1.2}Sr_{1.8}Mn_{1.7}Ru_{0.3}O_7$ Ruddlesden-Popper films on $SrTiO_3$, J. Cryst. Growth **311**, 1201 (2009).

[41] Y. F. Nie *et al.*, Atomically precise interfaces from non-stoichiometric deposition, Nat. Commun. **5**, 4530 (2014).

[42] G. M. De Luca *et al.*, Ubiquitous long-range antiferromagnetic coupling across the interface between superconducting and ferromagnetic oxides, Nat. Commun. **5**, 5626 (2014).

[43] Y. Tokura, T. Arima, H. Takagi, S. Uchida, T. Ishigaki, H. Asano, R. Beyers, A. I. Nazzal, P. Lacorre, and J. B. Torrance, New double-sheet copper oxide compounds with BiO or TIO bilayers, Nature (London) **342**, 890 (1989).

[44] M. Huvé, C. Martin, A. Maignan, C. Michel, G. Van Tendeloo, M. Hervieu, and B. Raveau, A new cuprate with mercury bilayers: The "2222" oxide $Hg_{2-x}M_xBa_2Pr_2Cu_2O_{10-\delta}$ (M = Cu, Pr), J. Solid State Chem. **114**, 230 (1995).

[45] P. Fisher, S. Wang, M. Skowronski, P. A. Salvador, M. Snyder, and O. Maksimov, Appl. Phys. Lett. **91**, 025290 (2007).

[46] N. M. Dawley, B. H. Goodge, W. Egger, M. Barone, L. F. Kourkoutis, and D. J. Keeble, Darrell G. Schlom Appl. Phys. Lett. **117**, 062901 (2020).

[47] J. Hemberger *et al.*, Structural, magnetic, and electrical properties of single crystalline $La_{1-x}Sr_xMnO_3$ ($0.4 < x < 0.85$), Phys. Rev. B **66**, 094410 (2002).

[48] O. Chmaissem *et al.*, Structural and magnetic phase diagrams of $La_{1-x}Sr_xMnO_3$ and $Pr_{1-y}Sr_yMnO_3$, Phys. Rev. B **67**, 094431 (2003).

[49] A. K. Jaiswal *et al.*, Direct observation of strong anomalous Hall effect and proximity-induced ferromagnetic state in $SrIrO_3$, Adv. Mater. **34**, 2109163 (2022).

[50] M. A. Laguna-Marco, D. Haskel, N. Souza-Neto, J. C. Lang, V. V. Krishnamurthy, S. Chikara, G. Cao, and M. Van Veenendaal, Orbital magnetism and spin-orbit effects in the electronic structure of $BaIrO_3$, Phys. Rev. Lett. **105**, 216407 (2010).

[51] S. Fujiyama, H. Ohsumi, T. Komesu, J. Matsuno, B. J. Kim, M. Takata, T. Arima, and H. Takagi, Two-dimensional heisenberg behavior of $J_{\text{eff}} = 1/2$ isospins in the paramagnetic state of the spin-orbital mott insulator Sr_2IrO_4, Phys. Rev. Lett. **108**, 247212 (2012).

[52] J. Matsuno, K. Ihara, S. Yamamura, H. Wadati, K. Ishii, V. V. Shankar, H. Y. Kee, and H. Takagi, Engineering a spin-orbital magnetic insulator by tailoring superlattices, Phys. Rev. Lett. **114**, 247209 (2015).

[53] L. Hao *et al.*, Two-dimensional $J_{\text{eff}} = 1/2$ antiferromagnetic insulator unraveled from interlayer exchange coupling in artificial perovskite iridate superlattices, Phys. Rev. Lett. **119**, 027204 (2017).

[54] L. Hao *et al.*, Giant magnetic response of a two-dimensional antiferromagnet, Nat. Phys. **14**, 806 (2018).

[55] S. Okamoto, Magnetic interaction at an interface between manganite and other transition metal oxides, Phys. Rev. B **82**, 024427 (2010).

[56] J. Salafranca and S. Okamoto, Unconventional proximity effect and inverse spin-switch behavior in a model manganite-cuprate-manganite trilayer system, Phys. Rev. Lett. **105**, 256804 (2010).

[57] Y. Lyanda-Geller *et al.*, Charge transport in manganites: Hopping conduction, the anomalous Hall effect, and universal scaling, Phys. Rev. B **63**, 184426 (2001).

[58] M. Bibes *et al.*, Anisotropic magnetoresistance and anomalous Hall effect in manganite thin films, J. Phys.: Condens. Matter **17**, 7332 (2005).

[59] W. J. Xu, B. Zhang, Z. X. Liu, Z. Wang, W. Li, Z. B. Wu, R. H. Yu, and X. X. Zhang, Anomalous Hall Effect in Fe/Gd Bilayers Europhys. Lett. **90**, 27004 (2010).

[60] W. J. Xu, B. Zhang, Z. Wang, S. S. Chu, W. Li, Z. B. Wu, R. H. Yu, and X. X. Zhang, Scaling law of anomalous Hall effect in Fe/Cu bilayers, Eur. Phys. J. B **65**, 233 (2008).

[61] Z. Fang, N. Nagaosa, K. S. Takahashi, A. Asamitsu, R. Mathieu, T. Ogasawara, H. Yamada, M. Kawasaki, Y. Tokura, and K. Terakura, The anomalous Hall effect and magnetic monopoles in momentum space, Science **302**, 92 (2003).

[62] M. Lee, Y. Onose, Y. Tokura, and N. P. Ong, Hidden constant in the anomalous Hall effect of high-purity magnet MnSi, Phys. Rev. B **75**, 172403 (2007).

[63] A. Neubauer, C. Pfleiderer, B. Binz, A. Rosch, R. Ritz, P. G. Niklowitz, and P. Böni, Topological Hall effect in the *A* phase of MnSi, Phys. Rev. Lett. **102**, 186602 (2009).

[64] N. J. Ghimire, A. S. Botana, J. S. Jiang, J. Zhang, Y. S. Chen, and J. F. Mitchell, Large anomalous Hall effect in the chiral-lattice antiferromagnet $CoNb_3S_6$, Nat. Commun. **9**, 3280 (2018).

[65] J. Ye, Y. B. Kim, A. J. Millis, B. I. Shraiman, P. Majumdar, and Z. Teanovic, Berry phase theory of the anomalous Hall effect: Application to colossal magnetoresistance manganites, Phys. Rev. Lett. **83**, 3737 (1999).